# The effect of silica oxide support on the catalytic activity of nickel-molybdenum bimetallic catalyst toward ethanol steam reforming for hydrogen production

Mohamed A. Elharati<sup>[a]</sup>, Kyung-Min Lee<sup>[b]</sup>, Sooyeon Hwang<sup>[c]</sup>, A. Mohammed Hussain<sup>[d]</sup>, Yohei Miura<sup>[e]</sup>, Song Dong<sup>[e]</sup>, Yosuke Fukuyama<sup>[e]</sup>, Nilesh Dale<sup>[d]</sup>, Steven Saunders<sup>[a]</sup>, Taejin Kim<sup>[b]\*</sup>, Su Ha<sup>[a]\*</sup>

- <sup>[a]</sup> Voiland School of Chemical Engineering and Bioengineering, Washington State University, Pullman, WA 99164-2710, USA
- <sup>[b]</sup> Department of Materials Science and Chemical Engineering, Stony Brook University, Stony Brook, NY 11794, USA
- <sup>[c]</sup> Center for Functional Nanomaterial, Brookhaven National Laboratory, Upton, NY 11973
- [d] Nissan Technical Centre North America, Farmington Hills, MI-48335, USA
- [e] Nissan Research Centre, Nissan Motor Corporation Limited, Kanagawa 237-8523, Japan

#### \*Corresponding Authors

Taejin Kim, Department of Materials Science and Chemical Engineering, Stony Brook University, Stony Brook, NY 11794, USA, taejin.kim@stonybrook.edu

Su Ha, Voiland School of Chemical Engineering and Bioengineering, Washington State University, Pullman, WA 99164-2710, USA, suha@wsu.edu

#### **ABSTRACT**

This paper investigates the effects of molybdenum promoter and silica oxide (SiO<sub>2</sub>) support morphology on the ethanol steam reforming (ESR) performance of Nickel-Molybdenum (NiMo) bimetallic catalysts. Ordered mesoporous SiO<sub>2</sub> (SBA-15) and commercial SiO<sub>2</sub> supports were used as the oxide support materials. The synthesized catalysts were prepared via the wet impregnation method and characterized via XRD, H<sub>2</sub>-TPR, BET, FTIR, and Raman techniques. This study shows that NiMo bimetallic catalyst supported on SBA-15 has superior catalytic activity and better coking resistance at an intermediate temperature of 600 °C than commercial SiO<sub>2</sub> supported catalysts. The presence of a uniform mesoporous structure of SBA-15 with an average pore diameter of  $\sim 2$  nm can obstruct the carbon formation, leading to improved coking resistance. The catalytic enhancement of NiMo bimetallic catalysts toward ESR can also be linked to the ability of Mo promoter in enhancing the interaction between NiMo nanoparticles and SiO<sub>2</sub> support materials and restraining agglomeration of Ni nanoparticles, which results in further improvement of NiMo nanoparticle dispersion and inhibit its sintering. The NiMo bimetallic catalysts supported on SBA-15 illustrated the high H<sub>2</sub> yield of ~54% and carbon conversion of ~89% with the excellent stability for ESR performed at 600 °C and the steam-to-carbon ratio of 2 over 65 hours.

**Key Words**: Ethanol steam reforming (ESR), Nickel-Molybdenum (NiMo), Ordered mesoporous SiO<sub>2</sub> (SBA-15), Raman, Coke formation, Hydrogen production

#### 1. Introduction

Searching for alternative and renewable energy sources is one of the most pursued focused research topics due to the CO<sub>2</sub> emission and environmental issues associated with using fossil fuels. Hydrogen (H<sub>2</sub>) technology is the most promising one among the proposed renewable energy technologies because it only produces the water as its byproduct when it combusts. However, ~ 95% of H<sub>2</sub> is currently produced by the steam reforming of natural gas, accompanied by a significant net CO<sub>2</sub> emission.<sup>[1, 2]</sup> Bioethanol is an attractive renewable fuel to generate green H<sub>2</sub> and syngas (CO and H<sub>2</sub>) via its steam reforming due to its relatively high hydrogen content, harmlessness, easy storage, and ample availability.<sup>[3]</sup> The CO<sub>2</sub> released from the ethanol reforming process could be converted into additional biomass via photosynthesis reaction, and this biomass could be converted into bioethanol. Hence, ethanol steam reforming (ESR) could be a viable future technology for producing the green H<sub>2</sub>,<sup>[2, 4]</sup> and it is expected to reduce the demand for fossil fuels and the emission of environmental pollutants.

Various noble metals like Rh and Pt have been utilized by supporting them on silica for efficiently catalyzing ESR. However, these noble metals are very expensive, and it is highly desired to design noble metal-free high-performance ESR catalysts <sup>[5-8]</sup>. Considering their low costs and competitive catalytic activities compared to noble metal catalysts, 3d-transition metal catalysts are promising alternative candidates that have been investigated for the ESR in the last two decades. <sup>[2,4,9]</sup> Among the transition metal catalysts, the Ni-based catalyst proved to effectively cleave O–H, C–C, and C-H bonds of ethanol or ethanol derivatives, such as acetates or ethanoxies. <sup>[10-12]</sup> However, the supported mono-metallic nickel (Ni) catalyst, such as Ni/Al<sub>2</sub>O<sub>3</sub> <sup>[13]</sup> and Ni/SiO<sub>2</sub>, <sup>[14,15]</sup> typically leads to rapid deactivations caused by the Ni nanoparticle sintering and carbon deposition. <sup>[16-18]</sup> The bimetallic NiMo catalysts have been studied in many catalytic

reactions such as ethanol steam reforming, [19, 20] dry methane reforming, [21] isooctane partial oxidation, [22] and hydrodesulfurization [23, 24] with an excellent coking resistance. This improved coking resistance of the bimetallic NiMo catalysts was explained in terms of modifying their electronic structure. The density functional theory (DFT)-based calculation showed that the bimetallic NiMo cluster over yttria-stabilized zirconia (YSZ) support is more positively charged than the monometallic Ni cluster over YSZ support, especially near the Mo atom. [25] The bimetallic NiMo catalysts with this unique electronic structure could be responsible for their improved coking resistance toward the partial oxidation of gasoline by obstructing the mechanistic pathways for carbon formation (i.e., carbon nucleation and carbon accumulation). Youn, M.H. *et al.* [26] and Bkour, Q. *et al.* [22, 25] also reported that the addition of Mo promoter prevents the Ni nanoparticles' growth and leads to high dispersion of NiMo over the supports.

Mesoporous silica (SBA-15) support has received significant attention as a promising support material and broadly studied for dry methane reforming [21, 27] and hydrodesulfurization [24] due to their synchronized mesoscale channels, a large pore volume (0.5-1 cm³/g), high surface areas in the range of 500-800 m²/g, and high thermal and chemical stabilities [28]. Delgado, A.D., et al. [23] studied the effects of the morphology of support materials, such as mesoporous and non-porous SiO<sub>2</sub>, on the hydrodesulfurization (HDS) activity. They reported that the texture properties of ordered-mesoporous SiO<sub>2</sub> (KIT-6) were the main reason for the induction of high dispersion of NiMoS stack. Consequently, the NiMo/KIT-6 catalyst showed a factor of two higher catalytic activity toward the HDS reaction than that of the NiMo/SiO<sub>2</sub> catalyst. To the best of our knowledge, there is a lack of studies for elucidating the effect of the silica morphology on the coking resistance of the NiMo bimetallic catalyst in ESR conditions. In this study, the mesoporous SBA-15 with the uniform pore size (~2 nm) and commercial SiO<sub>2</sub> with the broader pore size

distribution and bigger average pore size than 2 nm were employed as a support material for the NiMo bimetallic nanoparticles to determine how the ordered-mesoporous structure of silica support affects the ESR performance and coking resistance of NiMo nanoparticles under the harsh ESR operating conditions. The main objective of our research is to synthesize the catalyst that can be integrated into the metal-supported Solid Oxide Fuel Cell (SOFC) system so that we can directly feed the ethanol fuel into the fuel cell and produce electrical power. The ideal operating temperature of metal-supported SOFCs is 600 °C. Because the focus of our catalyst study is to apply it to the metal-supported SOFC, we have investigated the catalytic performance of our catalyst samples at 600 °C.

## 2. Experimental section

## 2.1. Catalyst synthesis

NiMo silica-supported catalysts were prepared via a wet impregnation (WI) method. Nickel nitrate hexahydrate (Ni(NO<sub>3</sub>)<sub>2</sub>.6H<sub>2</sub>O, 1.37 g) and ammonium molybdate tetrahydrate ((NH<sub>4</sub>)<sub>6</sub>Mo<sub>7</sub>O<sub>24</sub>.4H<sub>2</sub>O, 0.044 g) were mixed and dissolved in 30 ml of aqueous ethanol solution under the stirring condition to form a homogenous precursor solution mixture. A 0.7 g of either as-received silica mesoporous SBA-15 (Sigma-Aldrich, particle size < 150 μm, pore size of 4 nm, hexagonal pore morphology) or SiO<sub>2</sub> catalyst support (Alfa Aesar 43860, 1/8`` Pellets) grounded into powder (< 0.5 mm mesh diameter) was added into a homogenous solution slowly. The resultant mixture was kept under the stirring condition at 50 °C to evaporate the aqueous ethanol solution and obtain a greenish slurry. The greenish slurry went through a drying process overnight (~ 12 hours) at 80 °C in a controlled furnace. The dried solid powder was calcined at 600 °C for 3 hours at static air and a ramping rate of 5 °C/min. The calcined powder was ground and reduced

before the ESR reaction at 700 °C for 2 hours under flowing H<sub>2</sub> gas (50 ml/min), which was selected based on our H<sub>2</sub>-TPR results. This reduction temperature of 700 °C is selected based on our H<sub>2</sub>-TPR and less than melting temperature (1425 °C).<sup>[29]</sup> For comparison, the NiMo without the support and the supported mono-metallic catalysts (i.e., Ni/SBA-15 and Ni/SiO<sub>2</sub>) were also synthesized as references via the WI method. **Table 1** illustrates the preparation condition of each catalyst sample. The catalyst samples followed the calcination and reduction treatments as described in **Table 1** and referred them as "Fresh" samples.

**Table 1**. The preparation condition of synthesized catalysts

Catalysts	Ni wt. %	Mo wt. %	Si wt. %	Calcination	Reduction
NiMo	92	8	0	600 °C for 3 hr	700 °C for 2 hr
NiMo/SBA-15	27.6	2.4	70		
Ni/SBA-15	28.3	0	71.70		
Mo/SBA-15	0	3.3	96.4		
Ni/SiO <sub>2</sub>	28.3	0	71.70		
NiMo/SiO <sub>2</sub>	27.6	2.4	70		

#### 2.2. Catalyst characterizations

To characterize the crystalline phases of the fresh (i.e., calcined and reduced samples) and spent samples, the X-ray diffraction (XRD) analysis was performed at 40 kV and 15 mA via the Rigaku Miniflex 600 diffractometer with Cu Kα radiation. The XRD patterns were recorded at a scan rate of 1°/min with a scan step size of 0.01° in a range of 2θ from 20° to 60°. The XRD results were analyzed via Rigaku PDXL XRD analysis software.

High angle annular dark-field-scanning transmission electron microscopy (HAADF-STEM) images and STEM-energy dispersive X-ray spectroscopy (STEM-EDS) elemental maps were acquired with a Thermo-Fisher Talos F200X. HAADF and secondary electron (SE) image pairs were obtained simultaneously using a Hitachi HD2700C dedicated STEM with a probe Cs corrector. Both electron microscopes were operated at an accelerating voltage of 200 kV.

A chemisorption system (ChemiSorb 2720, Micromeritics) was used to perform hydrogen temperature-programmed reduction (H<sub>2</sub>-TPR) measurements. A 100 mg of the synthesized catalyst (i.e., the catalyst sample that was only calcined) was loaded into a quartz U-tube and pretreated with He/N<sub>2</sub> gas at flowrate 50 sccm while ramping temperature to 300 °C with a ramping rate of 10 °C/min. After cooling down the samples back down to 25 °C, the 10 vol. % H<sub>2</sub>/He gas mixture was then introduced at flowrate 50 sccm, and the temperature was ramped from 25 to 900 °C at a ramping rate of 10 °C/min to determine the reducibility peak of the samples.

Before the Brunauer–Emmett–Teller (BET) analysis, the fresh synthesized samples were degassed at 300 °C for 4 hours under vacuum to remove impurities and volatiles. The specific surface area measurements, the porosity of synthesized samples, and pore size distribution were obtained via the N<sub>2</sub> adsorption-desorption isotherms, which were recorded on the Quantachrome NovaWin ©1994-2007, Quantachrome Instruments v10.0 at 77.3 K. The mesopore size distributions from the adsorption branch was calculated via the Barrett–Joyner–Halenda (BJH) method.

Fourier transform infrared (FTIR) spectra were collected with a Nicolet<sup>™</sup> iS50 FTIR spectrometer (Thermo Fisher Scientific) equipped with an attenuated total reflectance (ATR) accessory. The FTIR of the fresh, calcined, and spent samples were collected in the wavenumber range of 400-4000 cm<sup>-1</sup> at a resolution of 4 cm<sup>-1</sup> and 32 scans.

Raman spectrometer (Horiba-Jobin XploRA<sup>TM</sup> PLUS Confocal Raman Microscope) equipped with 532nm laser was utilized to record the Raman spectra of the carbon phase on the spent samples. The Raman spectra were collected in the 1000-2000 cm<sup>-1</sup> Raman shift regions. The spectral acquisition time was 10 seconds, and each spectrum was accumulated from 60 scans.

#### 2.3. The catalytic activity of synthesized catalysts toward ESR

The isothermal fixed-bed reactor configuration, depicted in Fig. 1, was used to determine the catalytic activity of ESR. The synthesized catalyst (50±0.001 mg) was sandwiched between two layers of quartz wool, while the vaporizer (3±0.1 g of silicon carbide (SiC)) was placed in front of the catalyst layer. It should be noted that no ESR activity was observed with SiC or under the blank test (without catalyst) condition. A K-type thermocouple (Omega) was located closely at the catalyst layer to maintain its temperature at 600 °C for the ESR experiment. The SiC layer temperature was around  $100 \pm 3$  °C. The chiller was set up at 4 °C to trap the condensable compounds (e.g., water and unreacted ethanol), whereas the gas chromatograph was equipped with two packed columns (Molecular Sieve 13X and HayeSep D) and a TCD detector to analyze the resulting dry gases such as H<sub>2</sub>, CO, CO<sub>2</sub>, and CH<sub>4</sub>. Before the ESR reaction, the calcined sample was reduced and activated by flowing 50 sccm of the pure H<sub>2</sub> at 700 °C for 2 hours. The temperature of the fixed-bed catalyst was dropped from 700 °C to 600 °C, while the  $N_2$  gas was fed at the flow rate of 86±5 sccm. Once the temperature of the catalyst layer reached at 600 °C, the 45 vol. % aqueous ethanol solution was introduced at the top of the quartz tube at the flow rate of 1.5 ml/h using a calibrated syringe pump under atmospheric pressure. [30] The weight-hourlyspace-velocity (WHSV) was calculated based on the mass flow rate of the reactants feeding into the reactor (including the carrier gas N<sub>2</sub>) and the loading mass of the synthesized catalyst. For the catalytic activity tests of all the samples, we fixed the WHSV at ~ 156 h<sup>-1</sup> (WHSV is calculated based on the total flow rate, which includes the flow rates of ethanol (0.68 ml/hr), water (0.82 ml/hr), and N2 carrier gas (5160 ml/hr)). The ethanol conversion, H2 yield, CO yield, and CO2 yield are calculated based on the following equations:

$$Conversion = \frac{n_{CO,Out} + n_{CO2,Out} + n_{CH4,Out}}{2(n_{Ethanol,In})} x 100$$
 (1)

$$H_2Yield = \frac{2(n_{H2,Out})}{6(n_{Ethanol,In}) + 2(n_{H2O,Stoichiometry})} x 100$$
 (2)

$$CO \text{ or } CO_2Yield = \frac{n_{CO,Out} \text{ or } n_{CO2,Out}}{2(n_{Ethanol,In})} x 100$$
(3)

where (n<sub>CO</sub>, O<sub>ut</sub>), (n<sub>CO2</sub>, O<sub>ut</sub>), (n<sub>CH4</sub>, O<sub>ut</sub>), (n<sub>H2</sub>, O<sub>ut</sub>), (n<sub>Ethanol</sub>, I<sub>n</sub>), and (n<sub>H2O</sub>, Stoichiometry) are CO molar flowrate out, CO<sub>2</sub> molar flowrate out, CH<sub>4</sub> molar flowrate out, H<sub>2</sub> molar flowrate out, ethanol molar flowrate in, and stoichiometry molar flowrate of H<sub>2</sub>O in, respectively. The ethanol conversion is evaluated based on the C1 carbon products (CO, CO<sub>2</sub>, and CH<sub>4</sub>).

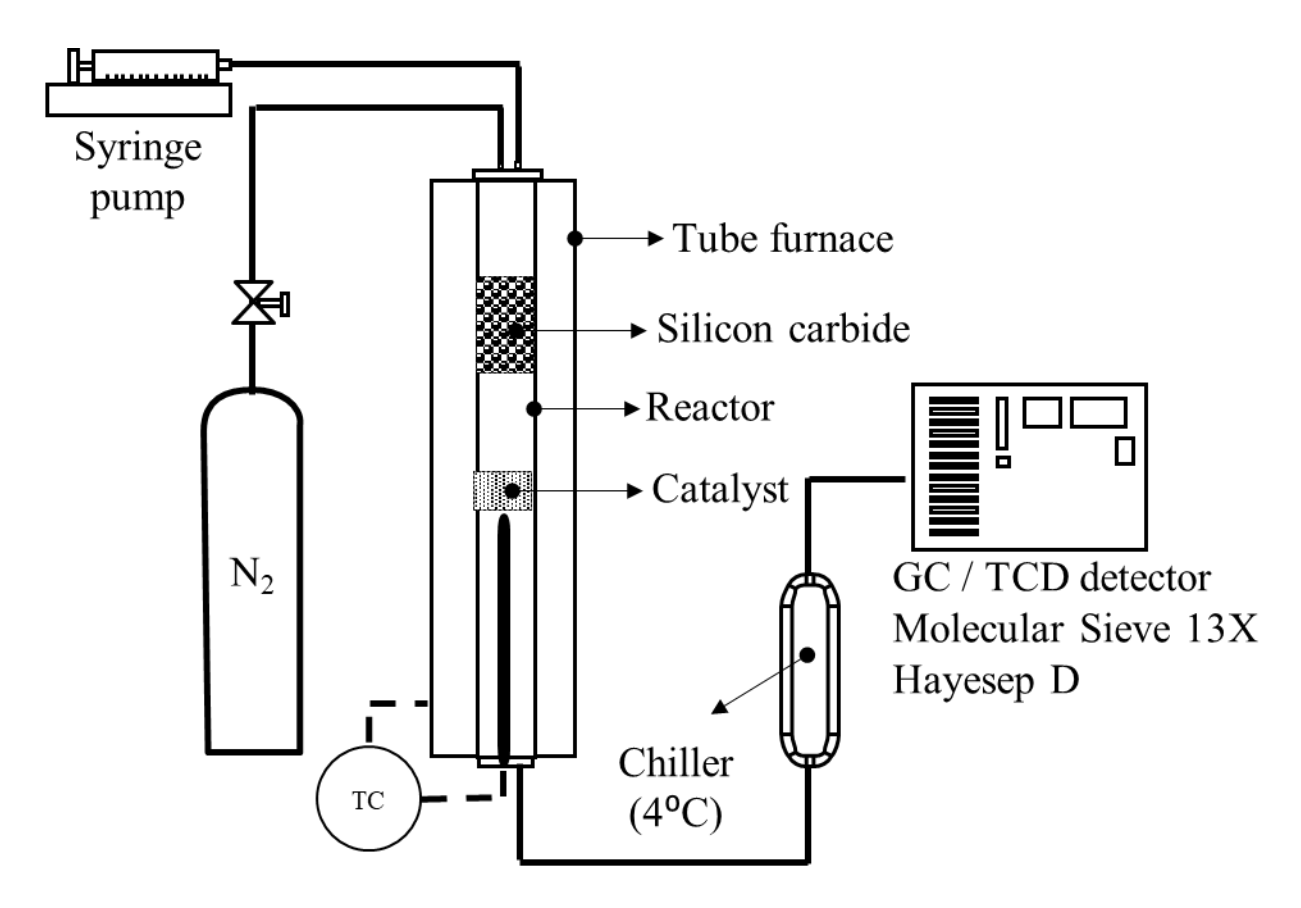


**Fig. 1** Schematic diagram of the experimental setup and fixed-bed reactor for testing the activity of the catalysts toward ESR.

#### 3. Results and discussion

### 3.1. X-ray diffraction (XRD) analysis

To determine the crystalline phases and average crystallite sizes of the fresh and spent synthesized catalysts, their XRD analysis was conducted. Note that the catalyst samples following the calcination and reduction treatments based on **Table 1** are referred to as "Fresh" samples. We first investigate the impact of heat treatments on the SAB-15 using XRD analysis as shown in Fig. S1. Fig. S1 exhibits the XRD patterns of SBA-15 as received and after the SBA-15 went through calcination and reduction processes. One can observe that SBA-15 maintains the XRD pattern after heat treatment, indicating the SBA-15 still preserve the mesoporous framework though there is a slight decline at peak centered at  $2\theta = 22^{\circ}$ . From Fig. 2 (A), the XRD patterns for silica (SBA-15 and SiO<sub>2</sub>)-supported NiMo catalysts show two diffraction peaks at 44.3° and 51.7°, which correspond to the (111) and (200) orientations of metallic Ni phase, respectively.<sup>[19]</sup> Comparing the XRD patterns of the Ni/SBA-15 sample, the metallic Ni diffraction peaks in the NiMo/SBA-15 spectrum are shifted toward lower values of 2θ, as shown in Fig. 2 (B). The Ni/SiO<sub>2</sub> and NiMo/SiO<sub>2</sub> samples also show a similar metallic Ni diffraction peak shift (See Fig. S2). These diffraction angle shifts indicate the expansion of the Ni lattice structure with the addition of Mo promoters.

We speculate that Mo atoms diffused into the Ni lattice structure during the catalyst synthesis process to form the solid solution phase. Because the Mo atoms (1.45 Å radius) are larger than the Ni atoms (1.35 Å radius), the Ni lattice structure expands as Mo atoms are incorporated into its crystalline structure. [25] The lattice parameters of the Ni phase with the face-centered cubic (fcc) structure were estimated based on the XRD data for the fresh samples of Ni/SiO<sub>2</sub>, NiMo/SiO<sub>2</sub>,

Ni/SBA-15, and NiMo/SBA-15. As shown in **Table 2**, the lattice parameter of the Ni phase is slightly increased as Mo is introduced to form the bimetallic NiMo catalysts.

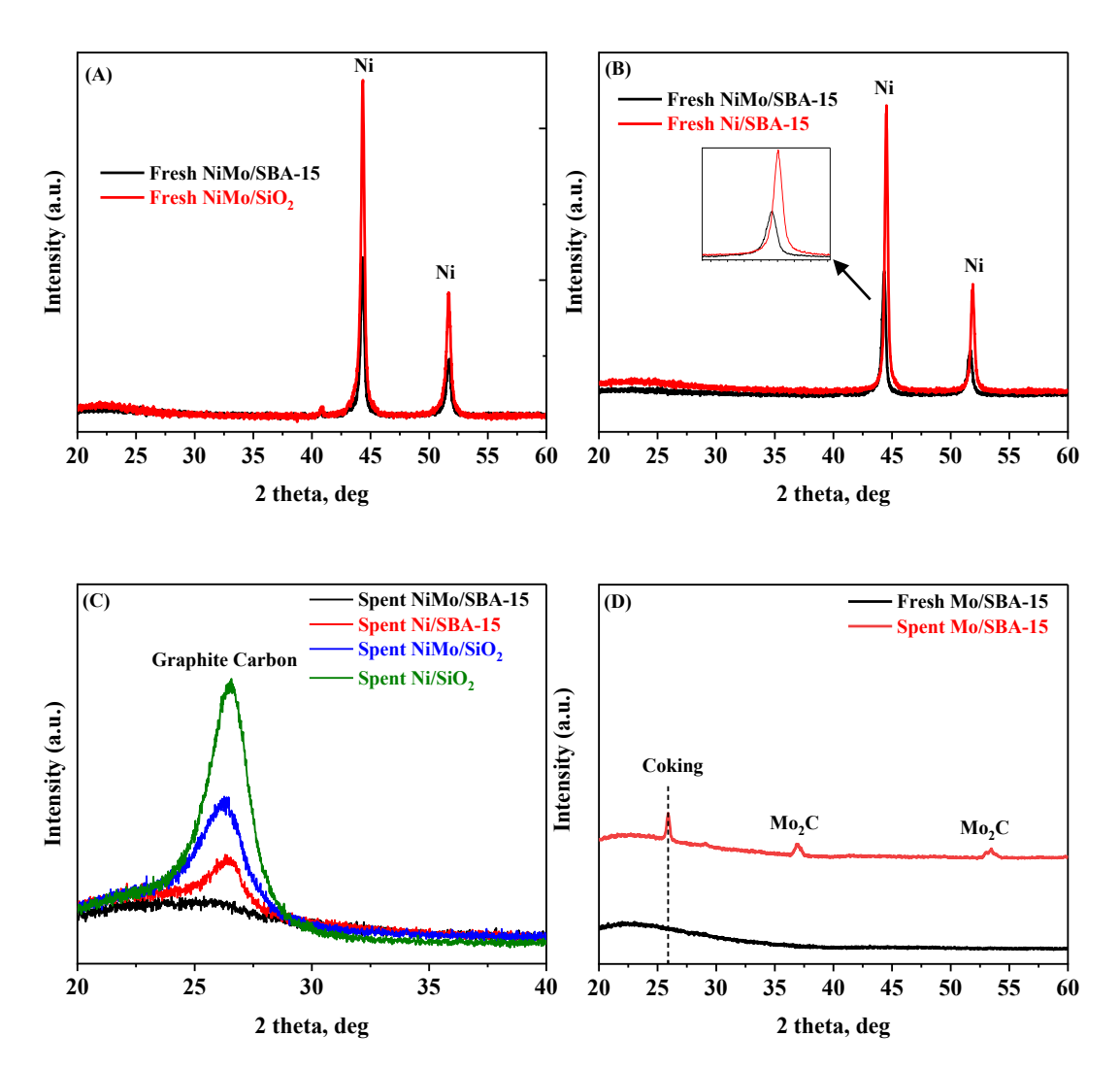


**Fig. 2** XRD data of (A) fresh samples of NiMo supported on SBA-15 and SiO<sub>2</sub>, (B) fresh samples of NiMo/SBA-15 and Ni/SBA-15, (C) spent samples of Ni/SiO<sub>2</sub>, Ni/SBA-15, NiMo/SiO<sub>2</sub>, NiMo/SBA-15, and (D) fresh and spent samples of Mo/SBA-15

The crystallite sizes of the metallic Ni phase at 44.55° peak for fresh samples of Ni/SiO<sub>2</sub>, Ni/SBA-15, and NiMo/SBA-15 were estimated employing the Scherrer equation, and results are summarized in **Table 2** as well. When we compare the average crystalline size of the metallic Ni phase for Ni/SiO<sub>2</sub> and NiMo/SiO<sub>2</sub> samples, it decreases from 20.74 to 19.03 nm as Mo

is introduced to Ni. Our previous research showed that the addition of Mo into the Ni lattice prevents the Ni nanoparticles from sintering during the calcination process.<sup>[22]</sup> A similar Mo effect on the Ni crystalline size is shown for Ni/SBA-15 and NiMo/SBA-15 samples. It is worthwhile to note that NiMo crystalline size was also affected by supports. As shown in **Table 2**, SBA-15 support further decreases the average crystalline size of Ni from 20.42 nm (NiMo/SiO<sub>2</sub>) to 15.6 nm (NiMo/SBA-15).

**Table 2**. Summary of Lattice Parameters and Average Crystallite Sizes of Metallic Ni Phase for Fresh Samples of Ni/SiO<sub>2</sub>, NiMo/SiO<sub>2</sub>, Ni/SBA-15, and NiMo/SBA-15

Supported catalyst	Ni/SiO <sub>2</sub>	NiMo/SiO <sub>2</sub>	Ni/SBA-15	NiMo/SBA-15
Lattice Parameters, Å	3.5158	3.5407	3.5237	3.5312
Average Crystalline size, nm	20.74	19.03	20.42	15.6

The XRD data of the spent Ni/SiO<sub>2</sub>, NiMo/SiO<sub>2</sub>, Ni/SBA-15, NiMo/SBA-15 samples for 24 hour-ESR test were compared. As shown in **Fig. 2** (C), the diffraction peak at  $2\theta = 26^{\circ}$ , which is assigned to graphitic carbon, is noticeable for all the spent samples. However, the addition of Mo significantly reduces the graphitic carbon peak intensity regardless of which support is used. Furthermore, its peak intensity for the spent NiMo/SiO<sub>2</sub> sample is much higher than that of the spent NiMo/SBA-15 sample, suggesting that NiMo/SBA-15 possesses an improved coking resistance and silica support morphology plays an important role for the graphitic carbon formation. The unique SBA-15 morphology can protect the NiMo nanoparticles from graphite (or coking) formation by physically protecting the metallic active sites within mesoporous cages, which limits coke formation.

**Fig. 2 (D)** shows the XRD patterns of the fresh and spent Mo/SBA-15 samples. For the fresh Mo/SBA-15 sample, the trace amount of Mo used to synthesize the sample and its

corresponding crystalline size of Mo phase are too small to be detected by XRD due to its detection limit. After running the ESR reaction at the S/C ratio of 2 and 600 °C for 24 hours, the spent Mo/SBA-15 sample shows the coke formation ( $2\theta = 26^{\circ}$ ) and formation of the Mo<sub>2</sub>C phase ( $2\theta = 37^{\circ}$  and 53°). The formation of the Mo<sub>2</sub>C phase was not observed in the case of spent NiMo/SBA-15 and NiMo/SiO<sub>2</sub> samples (**Fig. 2** (C)) indicating that Mo is firmly integrated within Ni lattice during the ESR reaction.

#### 3.2. HAADF-STEM analysis

Fig. 3 shows HAADF-STEM images and STEM-EDS elemental maps of both fresh and spent NiMo/SiO<sub>2</sub> and NiMo/SBA-15 samples. Regardless of what support materials we use, Mo atoms are highly dispersed over Ni particles. When we compared the fresh samples (Fig. 3 (A) and (B)), NiMo particles supported on SiO<sub>2</sub> are much bigger than NiMo particles supported on SBA-15. Following the ESR reaction over 24 hours, the spent NiMo/SiO<sub>2</sub> sample (Fig. 3 (C)) still shows large NiMo particles. For the spent NiMo/SBA-15 sample (Fig. 3 (D)), NiMo particles are still highly dispersed. For the fresh and spent NiMo/SBA-15 samples, NiMo particles can be presented both inside and outside the cage structure of SBA-15. Considering that electron microscopy generates projection images from 3D objects, HAADF-STEM and STEM-EDX maps may have a limit to distinguish if the NiMo particles are inside or outside the cage structure. Thus, we have collected secondary electron (SE) signals as well as HAADF-STEM images (Fig. S3). If the particles are inside the cage structure, they would not appear in SE images because SE signals are generated from the sample surfaces. According to Fig. S3, the small particles with a size of less than 2 nm only show up in HAADF-TEM images while absent in SE images. On the other hand, the large particles (~50 nm) appear on both HAADF-TEM and SE images. Thus, our image

analysis illustrates that the NiMo/SBA-15 catalyst possesses highly dispersed small NiMo nanoparticles (size less than 2 nm) within the mesoporous channels of SBA-15. Although most of the NiMo nanoparticles are within the mesoporous channel of SBA-15, there are still large NiMo particles out of the SBA-15 framework. Furthermore, the NiMo nanoparticles preserve their position inside the SBA-15 framework following the ESR reaction.

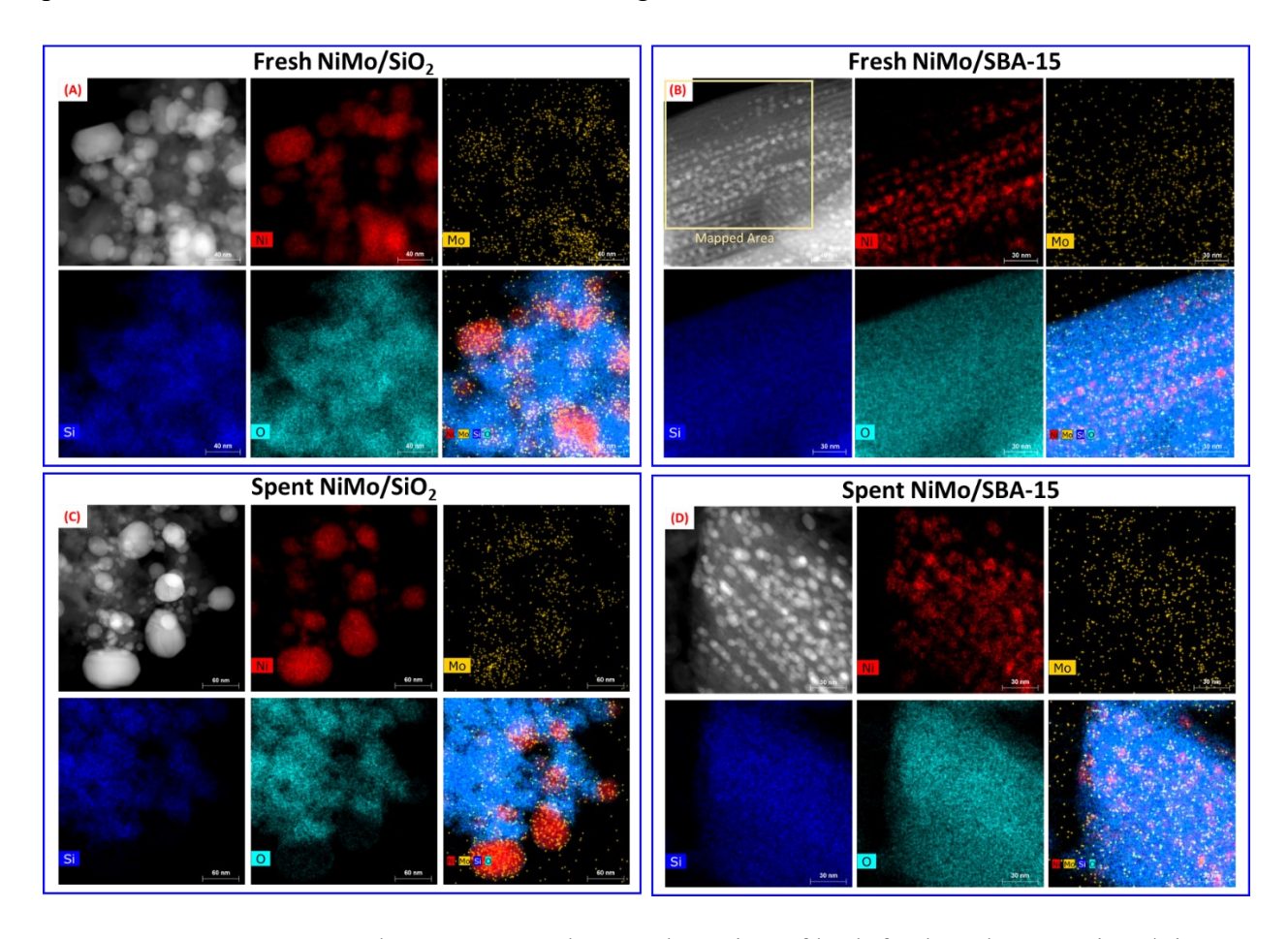


**Fig. 3.** HAADF-STEM and STEM-EDS elemental maping of both fresh and spent NiMo/SiO<sub>2</sub> and NiMo/SBA-15 samples

# 3.3. H<sub>2</sub>-TPR analysis

To investigate the nature of the interaction between NiMo nanoparticles and two different silica support materials, the H<sub>2</sub>-TPR analysis of calcined samples was conducted (i.e., the samples without the reduction step). The H<sub>2</sub>-uptake peak area and its location are depended on the degree

of the interaction of the catalyst sites with the oxide support materials. According to Fig. 4, the main reduction curves for the NiO<sub>x</sub> species for Ni/SiO<sub>2</sub> and Ni/SBA-15 samples appear between 225 and 400 °C, while they shift to a higher temperature between 325 and 550 °C for supported NiMo catalysts regardless of which silica support used. This result suggests that the addition of Mo increases the interaction between the metallic Ni sites and silica supports.

More interestingly, in addition to these main reduction peaks of the NiO<sub>x</sub> species (NiO<sub>x</sub>  $\rightarrow$  Ni) at 314 °C for Ni/SiO<sub>2</sub>, 300 and 340 °C for Ni/SBA-15, 499 °C for NiMo/SiO<sub>2</sub>, and 445 °C for NiMo/SBA-15, the shoulder peaks of the NiO<sub>x</sub> are also noticeable for the samples with SBA-15 supports. These shoulder peaks occur in the temperature range between 400 and 550 °C for Ni/SBA-15 sample and between 520 and 560 °C for NiMo/SBA-15 sample. One can notice that the Ni/SiO<sub>2</sub> and NiMo/SiO<sub>2</sub> samples do not show this shoulder peak. We speculate that these shoulder peaks originate from the NiO<sub>x</sub> particles impregnated within the hexagonal mesoporous structure of the SBA-15 with ~ 2 nm pore size (Pore size distribution data are shown in **Fig. 5**, and it is discussed in the following section). Thus, H<sub>2</sub>-TPR results indicate that there could be two different types of NiO<sub>x</sub> species in the Ni/SBA-15 and NiMo/SBA-15 samples: NiO<sub>x</sub> species presented at the outside and within SBA-15 mesoporous structure.

The reduction peak of MoO<sub>x</sub>/SBA-15 sample occurs at a wide range of temperatures, 250 - 900 °C, and its significant H<sub>2</sub> uptake took place at 450 °C and 750 °C (**Fig. S4** in Supporting Information), which indicates MoO<sub>x</sub> has a stronger interaction with oxide support material than the NiO<sub>x</sub>. Since there are no reduction peaks in the range between 700 and 900 °C, it is suggested that both MoO<sub>x</sub> species were not presented in the NiMo/SBA-15 and NiMo/SiO<sub>2</sub> samples. Based on the H<sub>2</sub>-TPR results, the appropriate reduction temperature of our catalyst samples is determined at 700 °C for 2 hours before the ESR experiments.

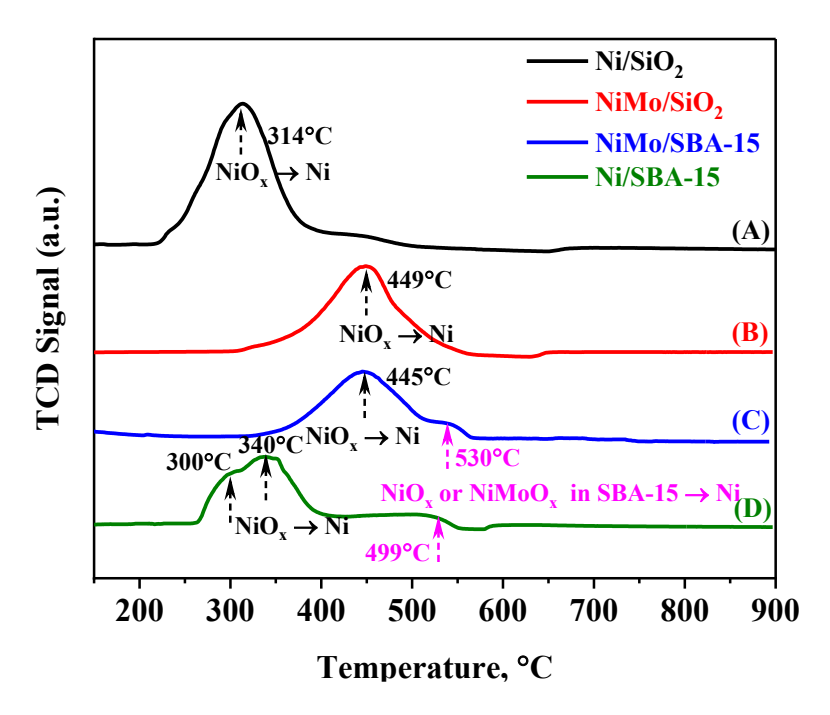


Fig. 4 TPR-H<sub>2</sub> of calcined (A) Ni/SiO<sub>2</sub>, (B) NiMo/SiO<sub>2</sub>, (C) NiMo/SBA-15, and (D) Ni/SBA-15.

## 3.4. Nitrogen physisorption analysis

The nitrogen adsorption-desorption isotherms of fresh samples along with the SiO<sub>2</sub> and SBA-15 supports were performed to characterize the pore structure using the BJH theory, as illustrated in **Fig. 5 (A)**. According to IUPAC classification, SBA-15 and NiMo/SBA-15 samples demonstrated a type IV isotherm with the hysteresis slope, leading to the presence of the well-ordered mesoporous morphology. Their isotherm curves logarithmically increased at the beginning associated with monolayer adsorption in mesoporous followed by its multilayer adsorption for gradual filling of well-defined mesopores framework and its subsequent capillary condensation. For NiMo/SBA-15 sample, the NiMo impregnation into SBA-15 leads to a slight change in the hysteresis slope compared to that of the as-received SBA-15 sample due to the infiltration and dispersion of metal ions within the mesopores channel of SBA-15.<sup>[31]</sup> Both SiO<sub>2</sub>

and NiMo/SiO<sub>2</sub> samples show a type III isotherm, indicating that the SiO<sub>2</sub> support material lacks mesoporous structures and possesses a bigger pore size than SBA-15.

As shown in Fig. 5 (B), both NiMo/SBA-15 and SBA-15 samples show a uniform pore-diameter distribution and a peak at 1.88 nm. These results indicate that the mesoporous structure of SBA-15 was well maintained after the infiltration of the NiMo species. This result also implies that the metallic particles are highly dispersed within the SBA-15 mesopores for NiMo/SBA-15.<sup>[32]</sup> Both SiO<sub>2</sub> and NiMo/SiO<sub>2</sub> samples demonstrate a lack of mesoporous structure, which is entirely different from SBA-15 and NiMo/SBA-15 samples. There is a small change in the large pore size distribution between SiO<sub>2</sub> and NiMo/SiO<sub>2</sub> due to the absence/presence of NiMo particles. The SiO<sub>2</sub> materials would agglomerate to form void spaces bigger than 2 nm. It seems that the presence of a large number of NiMo particles for the NiMo/SiO<sub>2</sub> sample would block some of these void spaces created by the agglomeration of SiO<sub>2</sub> materials. In the case of the unsupported NiMo sample, N<sub>2</sub> isotherm and pore size distribution results show a characteristic of the sample without well-defined pore structures.

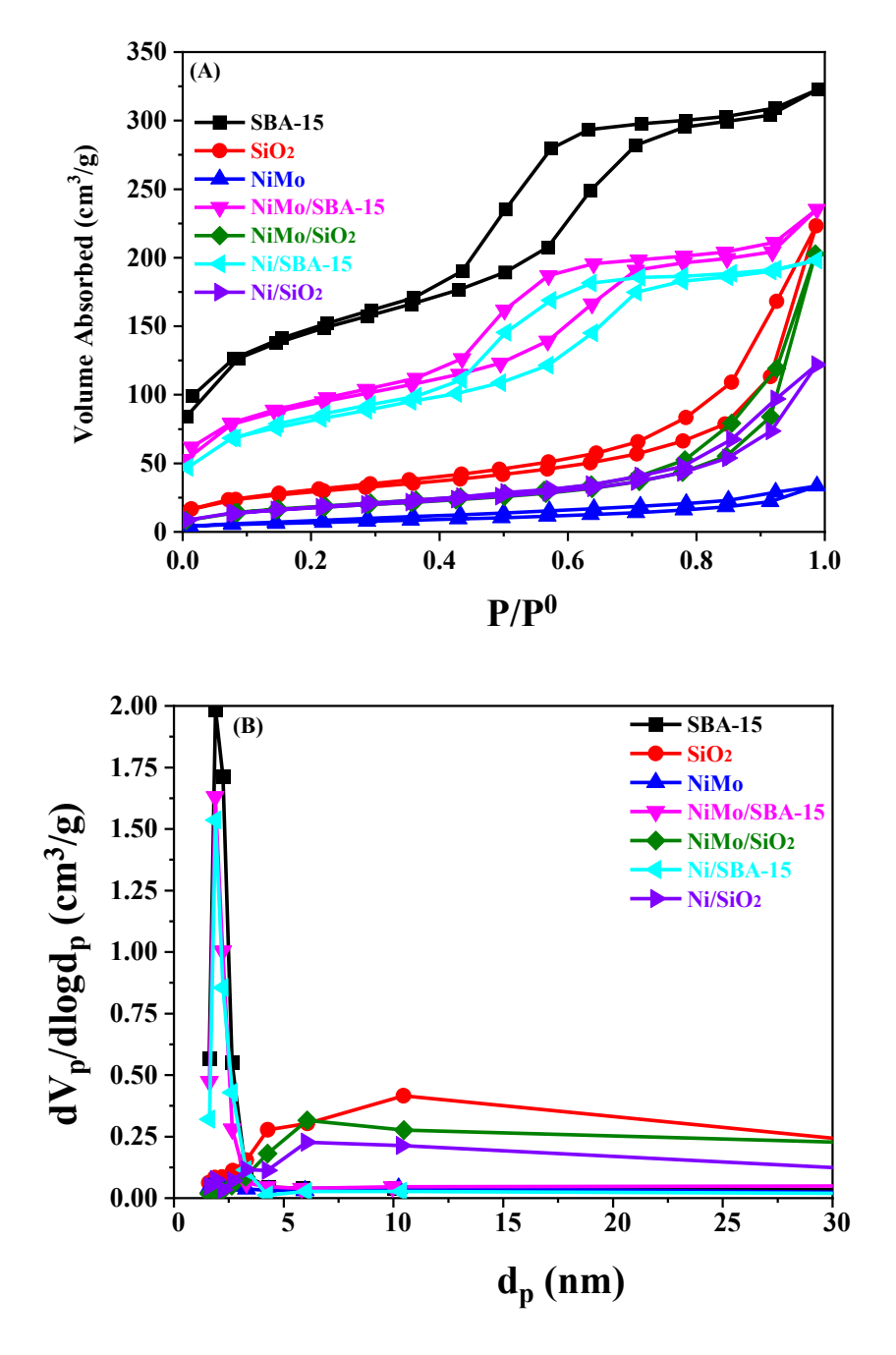


**Fig. 5** Nitrogen adsorption-desorption isotherms analysis (A) and pore size distribution (B) of SBA-15 as received, SiO2 as received, fresh NiMo, fresh Ni/SBA-15, fresh NiMo/SBA-15, fresh Ni/SiO<sub>2</sub>, and fresh NiMo/SiO<sub>2</sub> samples

Table 3 summarizes the BET analysis of as-received supports and fresh samples. The decreaseing of the specific surface area ( $S_{BET}$ ) and total pore volume ( $V_{Total}$ ) of fresh NiMo/SBA-15 sample compared to that of SBA-15 support confirm the introduction of the NiMo nanoparticles into the mesoporous cage of SBA-15. For NiMo/SiO<sub>2</sub> sample, the  $S_{BET}$  was decreased with adding the NiMo species compared to that of SiO<sub>2</sub> support, while the change of  $V_{Total}$  was not significant because of the lacking of mesoporous framework. Since the surface area of SiO<sub>2</sub> could not be changed during the calcination and reduction, the decreased surface area with adding of the NiMo species for NiMo/SiO<sub>2</sub> sample is caused by its increased total mass. Please note that the unsupported NiMo sample shows much lower  $S_{BET}$  and  $V_{Total}$  values than other samples. In summary, BET analysis indicates that the NiMo metallic nanoparticles were highly dispersed and well-embedded in the interior of the mesoporous channels of SBA-15, which would suppress the sintering of NiMo nanoparticles during the calcination process.

**Table 3.** The BET analysis of as-received SBA-15, as-received SiO<sub>2</sub>, fresh Ni and NiMo with and without silica oxide supports.

Samples	Specific surface area (m²/g)	Total pore volume (cm³/g)
SBA-15	426.7	0.50
NiMo/SBA-15	280.0	0.36
SiO <sub>2</sub>	94.4	0.34
NiMo/SiO <sub>2</sub>	57.9	0.31
NiMo	23.3	0.05

#### 3.5. Catalytic activity

The catalytic activities toward the ESR were conducted using 45% ethanol aqueous solution at temperature of 600 °C, the S/C ratio of 2, and the flow rate of 1.5 ml/hr. These are the typical operating conditions used for testing the metal-supported SOFC with ethanol fuel. A series of the synthesized catalysts including the unsupported NiMo, Ni/SBA-15, Mo/SBA-15,

NiMo/SBA-15, Ni/SiO<sub>2</sub>, and NiMo/SiO<sub>2</sub> were tested to study the effects of the Mo promoter and the mesoporous structure of the support on the catalytic activity and catalyst deactivation during the ESR reaction. The ESR performance of the reactor without loaded catalyst showed  $\sim 0.3\%$  carbon conversion, indicating there was neither ethanol thermal decomposition nor ESR reaction in these operating conditions without the catalysts.

Fig. 6 illustrates that the unsupported NiMo and Mo/SBA-15 samples could not show any catalytic performance for the ESR reaction. In the case of the unsupported NiMo samples, the Ni dispersion was poor, limiting its available active sites for the reaction. The Mo/SBA-15 sample demonstrated no catalytic activity toward the ESR reaction because Mo cannot trigger and break down the C-C bond. The Ni/SiO<sub>2</sub> and Ni/SBA-15 catalyst samples showed some activity toward the ESR reaction over the initial 5 hours, but their conversion decreased continuously to 0% due to the deactivation process. These catalytic performance data suggest that both Ni metallic site and support are required to activate the ESR reaction. Regardless of which silica support was used, the supported NiMo catalyst samples showed significantly improved activity and stability toward the ESR reaction compared to unsupported NiMo and supported Ni catalysts (

Fig. 6 (A)-(D)). For example, the conversion and  $H_2$  yield of NiMo/SBA-15 sample were increased up to  $\sim 90\%$  and  $\sim 54\%$ , respectively. The improvement of the ESR performance with the Mo addition to the metallic Ni could be originated from the enhanced dispersion of Ni nanoparticles, as evidenced by their decreased average crystalline sizes (**Table 2**).

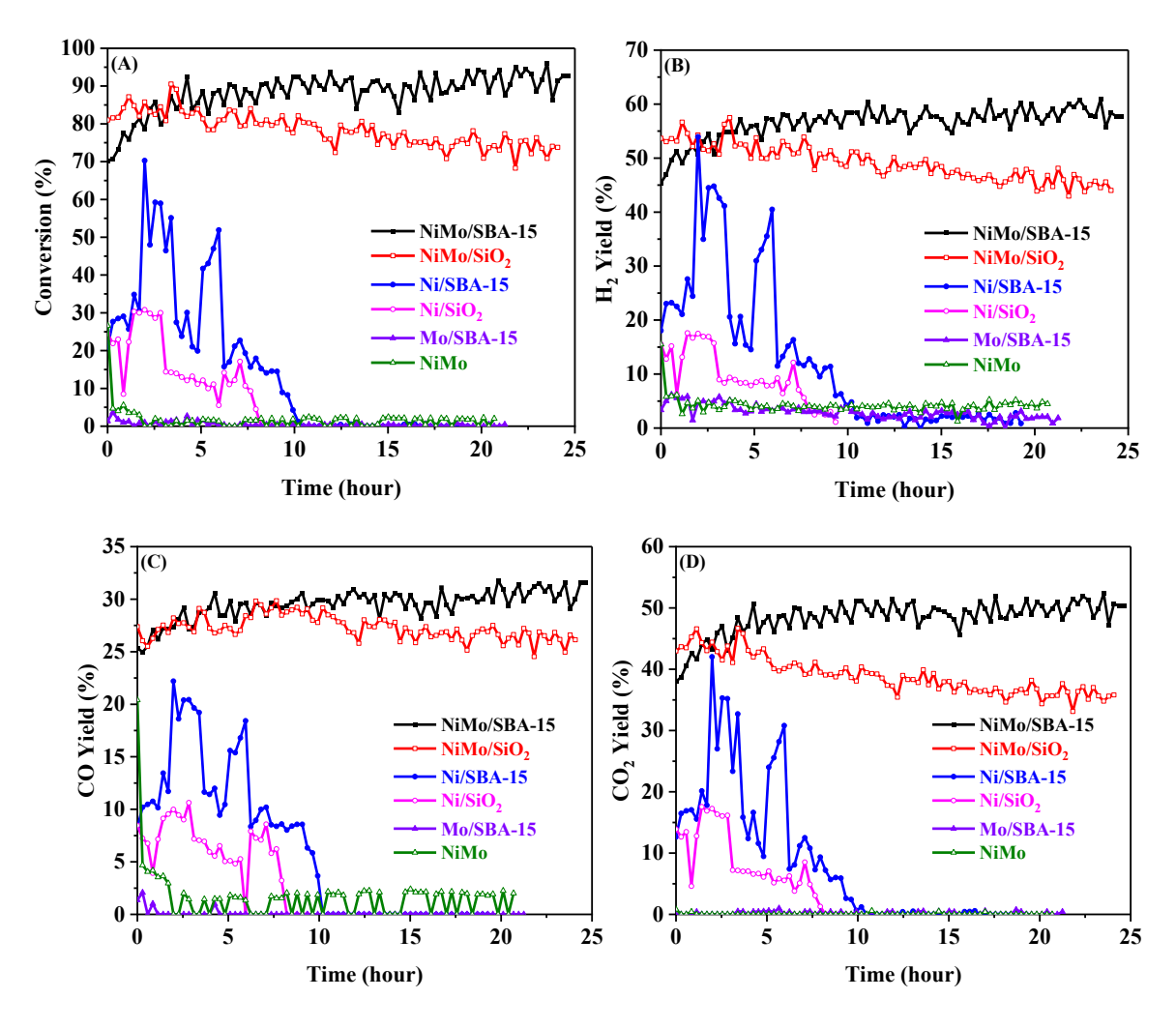


**Fig. 6** The ESR catalytic activity of NiMo, Ni/SBA-15, Mo/SBA-15, NiMo/SBA-15, Ni/SiO<sub>2</sub>, and NiMo/SiO<sub>2</sub> catalyst samples: (A) conversion, (B)  $H_2$  yield, (C) CO yield, and (D) CO<sub>2</sub> yield. The ESR experiments were performed for 24 hours at S/C = 2 with the catalyst mass of 50 mg, 600 °C, and ethanol solution flow rate of 1.5 ml/hr.

In addition to the increased catalytic activity toward the ESR due to its improved Ni dispersion over the support, the addition of Mo into Ni particles can also modify Ni nanoparticles' electronic structure.<sup>[22, 25]</sup> Bkour, Q., *et al.* <sup>[25]</sup> used the DFT model to investigate the electronic

interactions between the Ni (or Ni-Mo) cluster and the YSZ slab in the most favorable configurations of Ni/YSZ and Ni-Mo/YSZ via a differential charge analysis. They also used a Bader charge analysis to quantitatively validate the integration of the electron cloud in the differential charge density analysis, where the Ni-Mo cluster is more positively charged than the pure Ni cluster, especially near the Mo atom. This data indicates the Ni-Mo cluster exists in a more stabilized form with a higher oxidation state as compared to the one in the absence of Mo when adsorbed on the YSZ slab. Both C-H bond cleavage and C-C coupling reactions are two main elementary reactions responsible for coke formation in typical fuel reforming reactions. Bkour, Q., et al. [25] reported that these two elementary reactions have higher activation barriers over the Modoped Ni catalyst site as compared to the pure Ni catalyst site without the Mo dopant. Hence, the electronic structure change of NiMo nanoparticles improved their catalytic activity and coking resistance for the hydrocarbon reforming reactions. [22, 25] For our present study, we used SBA-15 and SiO<sub>2</sub> supports (instead of YSZ), but we believe that similar electronic structure change would occur for our Ni-Mo clusters too. This ligand effect can also improve the NiMo/SiO<sub>2</sub> and NiMo/SBA-15 samples' catalytic activity and stability during the ESR reaction. Compared to the NiMo/SBA-15 sample, the NiMo/SiO<sub>2</sub> sample also exhibited a competitive initial catalytic activity, but it slowly deactivated over the 24 hours due to the carbon deposition, as evidenced by the XRD result (

**Fig. 6 (D)**). Unlike the NiMo/SiO<sub>2</sub> sample, the NiMo/SBA-15 sample maintained high initial activity over the 24-hour test. As shown in its corresponding XRD spectrum, the spent NiMo/SBA-15 sample showed a weaker intensity for the graphitic carbon phase compared to that of the spent NiMo/SiO<sub>2</sub> sample. Thus, it is evident that the morphology of silica support plays an essential role in influencing the catalyst coking for the ESR reaction. It is hypothesized that the

well-defined mesoporous channels of SBA-15 physically protected the NiMo nanoparticles from carbonaceous material deposition by limiting the excessive amount of ethanol molecules reaching the active sites. Additionally, the mesoporous structure of SBA-15 support could restrict the growth NiMo nanoparticles deposited within its mesoporous cages, leading to a lower degree of coking.

Based on the ESR data shown in

**Fig. 6**, we selected the NiMo/SBA-15 sample to investigate its stability for the long-term ESR reaction under the same experimental conditions. As shown in **Fig. 7**, the NiMo/SBA-15 sample exhibited high catalytic performance (~90% conversion and ~54% H<sub>2</sub> yield) and stability over 65 hours. This result suggests that NiMo/SBA-15 sample is a promising catalyst for the ESR reaction application.

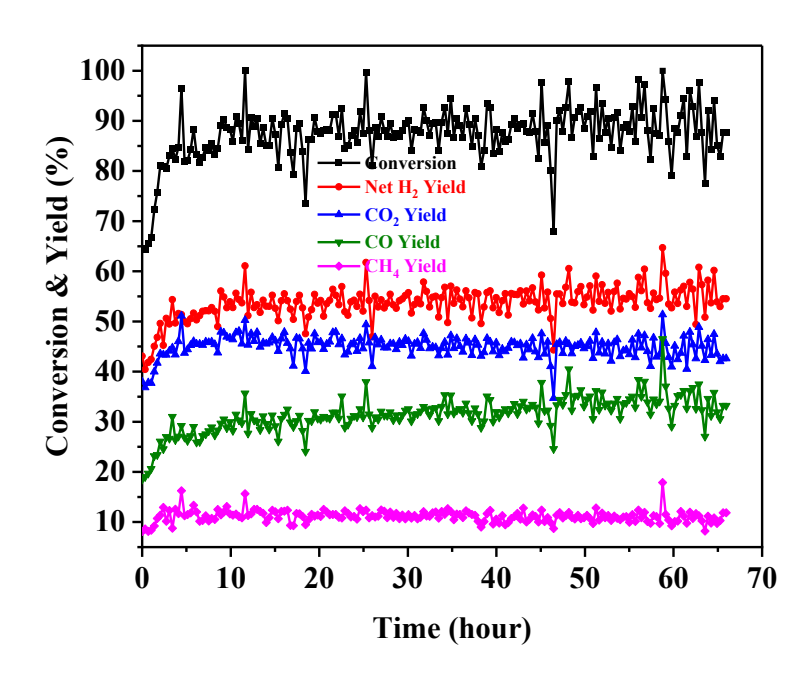


**Fig. 7** The ESR catalytic activity of NiMo/SBA-15 sample over 65 hours. The ESR experiment was performed for 24 hours at S/C = 2 with the catalyst mass of 50 mg,  $600 \, ^{\circ}$ C, and ethanol solution flow rate of 1.5 ml/hr.

#### 3.6. Fourier Transform Infrared (FTIR) and Raman spectroscopy analysis

The FTIR analysis was used to investigate further the molecular structure of fresh and spent NiMo/SiO<sub>2</sub> and NiMo/SBA-15 catalyst samples. As shown in Fig. 8 (A), all samples show the typical characteristic absorption peaks of silica material. The adsorption peaks at 449 cm<sup>-1</sup> (strong), 800 cm<sup>-1</sup> (medium), 970 cm<sup>-1</sup> (weak), and 1045 (strong)/1218 cm<sup>-1</sup> (weak) are associated with Si-O bending in silica network, Si-O-Si symmetric stretching, Si-O bending in silanol group, and Si-O-Si asymmetric stretching modes, respectively. [33-40] It is noted that -OH vibration modes, which could be shown in ~1650 cm<sup>-1</sup> (bending mode) and ~3500 cm<sup>-1</sup> (stretching mode) due to the physisorbed water and Si-OH Brønsted acidic site, were not observed in the samples' spectra. [36, 39] One can observe from the FTIR result that the NiMo/SBA-15 sample maintained similar absorption band structures in the wavenumbers corresponding to the silica material (i.e., 800 cm<sup>-1</sup>, 970 cm<sup>-1</sup>, and 1045~1071cm<sup>-1</sup>) after the calcination process, reduction process, and the ESR test. It suggests that the framework of SBA-15 support did not collapse during the catalyst preparation steps and the ESR test. In addition to the silica-related bands, the supported NiMo samples spectra contain a weak absorption peak at 560 cm<sup>-1</sup>, which is assigned to Ni-O vibration mode. [41]

Raman spectroscopy was used to identify the type of carbonaceous materials deposited on the surfaces of the spent NiMo/SiO<sub>2</sub> and NiMo/SBA-15 catalysts, as shown in **Fig. 8 (B)**. The two intense peaks appeared at ~1350 cm<sup>-1</sup> and ~1590 cm<sup>-1</sup>, which are associated with the disordered sp<sup>2</sup> carbon species (D-band) and graphitic carbon species (G-band), respectively.<sup>[25, 42-45]</sup> The Raman spectra of the spent NiMo/SiO<sub>2</sub> sample exhibited a higher intensity D to G ratio (I<sub>D</sub>/I<sub>G</sub>)

than that of the spent NiMo/SBA-15 sample. The Raman data indicates that the peak intensity of the D-band for NiMo supported on SiO<sub>2</sub> is much higher than that of NiMo supported on SBA-15. This suggests that the spent NiMo/SiO<sub>2</sub> sample possessed higher contents of amorphous carbon species than that of the spent NiMo/SBA-15 sample. This difference of D-band peak intensity and amount of amorphous carbon species formed for the spent NiMo supported on SiO<sub>2</sub> and SBA-15 could be related to the absence and presence of mesoporous structure of silica, respectively. We also have obtained the Raman spectra of spent Ni/SBA-15 and Ni/SiO<sub>2</sub> samples (**Fig. S5**). When the Raman spectra of the spent Ni/SiO<sub>2</sub> sample (or the spent Ni/SBA-15 sample) is compared to that of the spent NiMo/SiO<sub>2</sub> sample (or the spent NiMo/SBA-15 sample), the I<sub>D</sub>/I<sub>G</sub> ratio decreases with the addition of Mo atoms. Hence, the presence of Mo changes the coking reaction selectivity such that the formation of the graphitic carbon is more favorable over the formation of the amorphous carbon.

Based on the ESR activity, XRD, and Raman data of spent SiO<sub>2</sub>- and SBA-15-based catalyst samples, it is clear that the silica support morphology plays an important role in influencing the ESR performance of the supported Ni and NiMo catalysts. More specifically, the SBA-15 with the well-defined mesoporous structure improves the coking resistance of the Ni and NiMo catalyst by forming the lower degree of both the graphitic (XRD) and amorphous (Raman) carbon depositions. We speculate that the NiMo nanoparticles would be physically encapsulated within the mesoporous structure of SBA-15 support, resulting in the smaller size of NiMo particles which remain to be stable during the ESR reaction. These combined effects (i.e., the high sintering and coking resistance) would allow the high ESR performance over the 65 hours test.

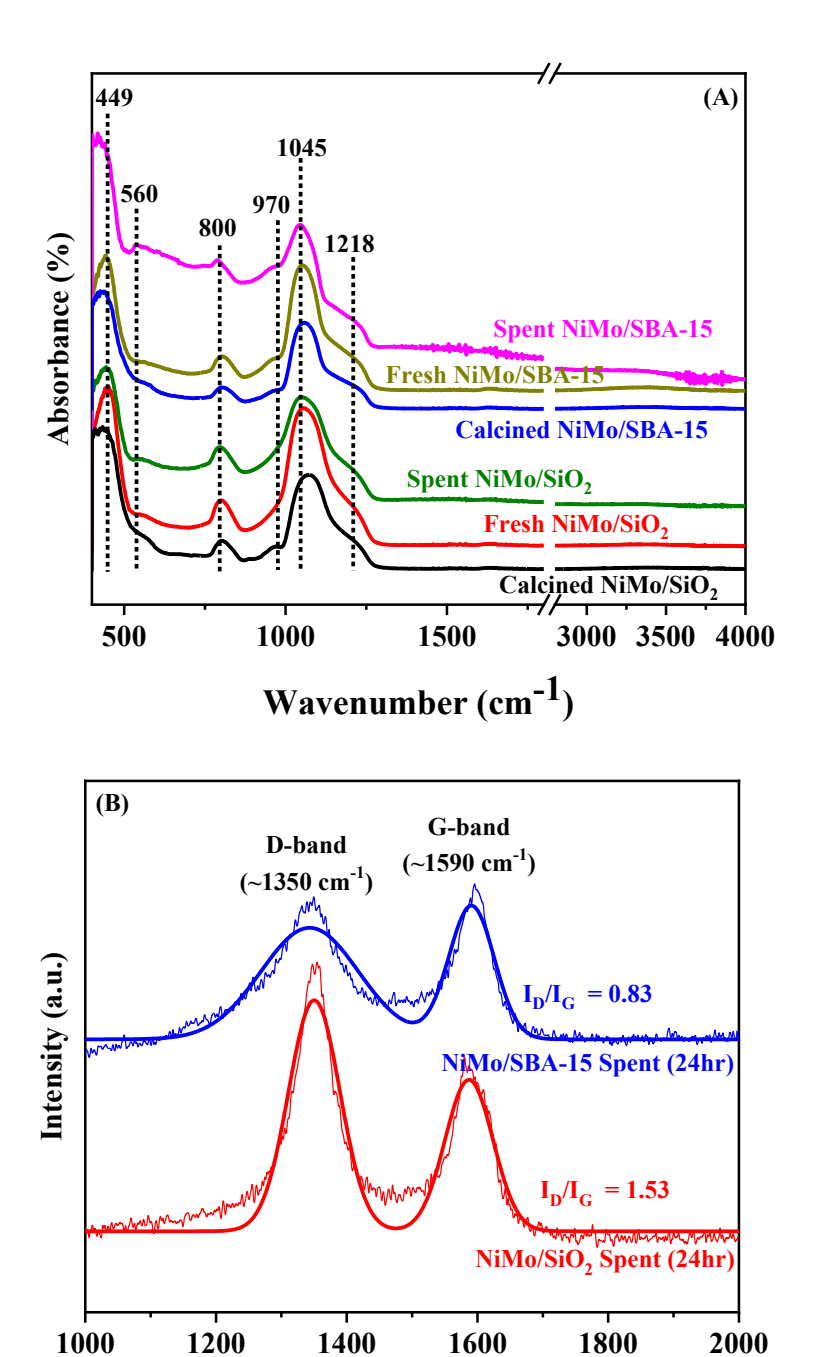


**Fig. 8** FTIR spectra (A) of fresh, calcined and spent NiMo/SiO<sub>2</sub> and NiMo/SBA-15 samples. and Raman spectra (B) of spent NiMo/SiO<sub>2</sub> and NiMo/SBA-15 samples. The ESR experiments were

Raman Shift (cm<sup>-1</sup>)

performed at S/C = 2 with the catalyst mass of 50 mg, 600 °C, and ethanol solution flow rate of 1.5 ml/hr.

## 3.7. TGA Analysis of Spent Catalyst Samples.

From the TGA data of spent Ni/SiO<sub>2</sub>, NiMo/SiO<sub>2</sub>, Ni/SBA-15, and NiMo/SBA-15 samples, both the weight and derivative of weight are plotted as a function of temperature in Fig. **S6.** From this TGA data, we approximate the degree of coking by estimating the % weight loss for each sample (i.e., there is a higher degree of coking as the % weight loss increases). As the temperature increases, the weight of all the spent samples slightly increases due to the oxidation of Ni and Mo metals. It is important to note that the spent NiMo/SBA-15 sample shows the highest weight increase, followed by the spent Ni/SBA-15, NiMo/SiO<sub>2</sub>, and N/SiO<sub>2</sub>. This order is the same as the order of the spent samples with the lowest degree of coking. It seems that the sample with a lower degree of coking allows a higher exposure of its metals to the air, which leads to a higher degree of metal oxidation and initial weight increase. As the temperature continuously increases, the weight of all the spent samples rapidly decreases due to the removal of their carbons via the carbon oxidation reaction. According to Fig. 9, the Ni catalyst supported on SBA-15 exhibits a lower degree of coking than the Ni catalyst supported on SiO<sub>2</sub>. This result indicates the crucial role of the mesoporous cage structure of SBA-15 support on improving the coking resistance of Ni catalyst, which was confirmed by TEM, XRD, and Raman analysis. Furthermore, the addition of Mo further enhances the coking resistance for both NiMo/SiO<sub>2</sub> and NiMo/SBA-15 catalyst samples; however, the NiMo/SiO<sub>2</sub> sample still shows a more significant amount of carbon than the NiMo/SBA-15 sample.

The derivative peak of the TGA profile shows that the spent Ni/SiO<sub>2</sub> has both broad and sharped peaks in the range between 425°C - 625°C, indicating there are different types of carbon formed during the ESR reaction. As Mo atoms are introduced to Ni (e.g., NiMo/SiO<sub>2</sub> and NiMo/SBA-15), the sharped peak disappears while the broad peak shifts to the higher temperature. We speculate that the broad peak is associated with the amorphous carbons, while the sharp peak is associated with the graphitic carbons. This result suggests that the type of carbon forms (e.g., amorphous carbon versus graphitic carbon) and carbon formation kinetics over our catalyst sample is strongly influenced by the addition of Mo atoms.

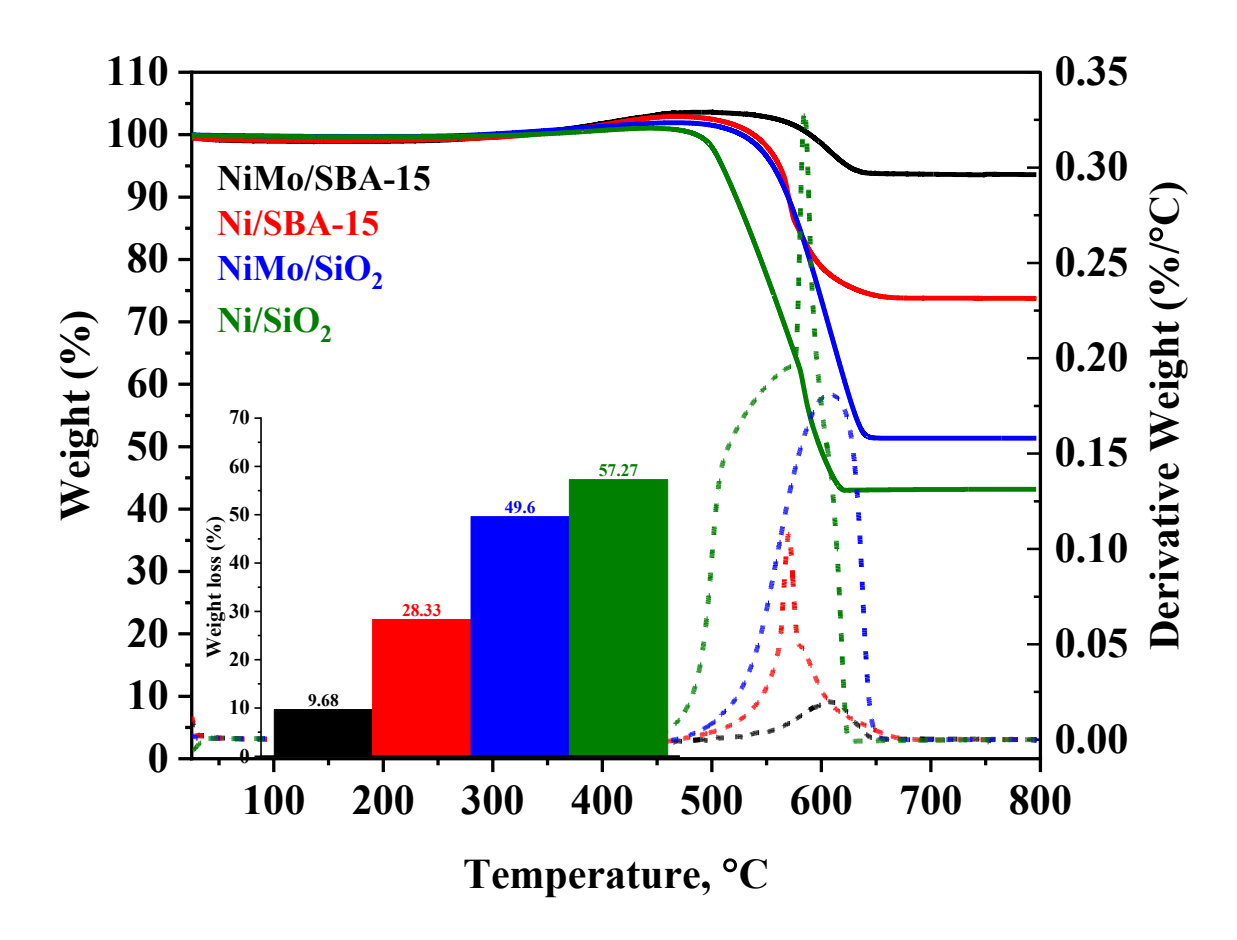


**Fig. 9** TGA analysis of spent samples of Ni/SiO<sub>2</sub>, NiMo/SiO<sub>2</sub>, Ni/SBA-15, and NiMo/SBA-15. The ESR experiment was performed at a temperature of 600 °C, S/C ratio of 2, and flowrate of 1.5 ml/min.

#### **Conclusions**

In this work, we have studied the ethanol steam reforming (ESR) reaction over the unsupported, SiO<sub>2</sub> supported, and SBA-15 supported Ni-based catalysts with and without Mo promoters. Among NiMo, Ni/SiO<sub>2</sub>, NiMo/SiO<sub>2</sub>, Ni/SBA-15, and NiMo/SBA-15 catalyst samples that we have tested for the ESR at the S/C ratio of 2 and 600 °C, the NiMo/SBA-15 catalyst demonstrated the highest catalytic stability. This can be explained by the high dispersion of the bimetallic NiMo nanoparticle within the mesoporous cages of SBA-15, which inhibits the nanoparticle growth and the formation of carbon depositions on the active sites. Due to these unique properties of the NiMo/SBA-15 catalyst, it exhibited high ESR performance (e.g., ~90% conversion and ~50% H<sub>2</sub> yield) and remained stable over 65 hours.

#### **Conflicts of Interest**

The authors declare no conflict of interests that could lead to impact the reported work in this paper.

## Acknowledgments

This material is based upon work supported by the United State National Science Foundation under award number CBET- 2050691. The authors acknowledge the O.H. Reaugh Laboratory at Washington State University for using its facility to perform activity tests of the synthesized NiMo supported and unsupported silica oxide samples. The authors also acknowledge Stony Brook University (SBU) for using their expertise and facilities and running Raman, FTIR, and BET analysis of the synthesized NiMo supported and unsupported silica oxide samples. Mohamed A. Elharati gratefully acknowledges the Libyan Ministry of Higher Education for supporting his Ph.D. program. This research used resources of the Center for Functional Nanomaterials (CFN), which is a U.S.

Department of Energy Office of Science User Facility, at Brookhaven National Laboratory under Contract No. DE-SC0012704.

#### References

- 1. Mazloomi, K. and C. Gomes, *Hydrogen as an energy carrier: Prospects and challenges.* Renewable and Sustainable Energy Reviews, 2012. **16**(5): p. 3024-3033.
- 2. Haryanto, A., et al., *Current Status of Hydrogen Production Techniques by Steam Reforming of Ethanol: A Review.* Energy Fuels, 2005. **19**(5): p. 2098-2106.
- 3. Ni, M., et al., *An overview of hydrogen production from biomass.* Fuel Processing Technology, 2006. **87**(5): p. 461-472.
- 4. Hou, T., et al., *Hydrogen production from ethanol reforming: Catalysts and reaction mechanism.* Renewable and Sustainable Energy Reviews, 2015. **44**: p. 132-148.
- 5. Ito, S.-i. and S. Kameoka, *Effect of strong metal-oxide interaction on low-temperature ethanol reforming over Fe-promoted Rh/SiO*<sub>2</sub> catalyst. Applied Catalysis A: General, 2021. **617**: p. 118113-118119.
- 6. Sun, C., et al., Yolk-shell structured Pt-CeO2@Ni-SiO<sub>2</sub> as an efficient catalyst for enhanced hydrogen production from ethanol steam reforming. Ceramics International, 2018. **44**(2): p. 1438-1442.
- 7. Palma, V., et al., Enhancing Pt-Ni/CeO<sub>2</sub> performances for ethanol reforming by catalyst supporting on high surface silica. Catalysis Today, 2018. **307**: p. 175-188.
- 8. Palma, V., et al., Influence of Catalytic Formulation and Operative Conditions on Coke Deposition over CeO2-SiO2 Based Catalysts for Ethanol Reforming. Energies, 2017. **10**(7): p. 1030.
- 9. Mattos, L.V., et al., *Production of hydrogen from ethanol: review of reaction mechanism and catalyst deactivation.* Chemical Reviews, 2012. **112**(7): p. 4094-4123.
- 10. Gates, S.M., J.N.R. Jr., and J.T.Y. Jr., *Bond activation sequence observed in the chemisorption and surface reaction of ethanol on Ni(111)*. Surface Science, 1986. **171**(1): p. 111-134.
- 11. Xu, J., et al., Ethanol decomposition on Ni(111): observation of ethoxy formation by IRAS and other methods. Surface Science, 1991. **256**(3): p. 288-300.
- 12. Rodriguez, W.X.Z.L.A.C.J.-P.S.D.S.G.Z.D.S.E.A.S.J.A., Steam Reforming of Ethanol on Ni/CeO<sub>2</sub>: Reaction Pathway and Interaction between Ni and the CeO<sub>2</sub> Support. ACS Catalysis, 2013. **3**(5): p. 975–984.
- 13. Helveg, J.S.J.A.P.G.S., *Sintering of nickel catalysts: Effects of time, atmosphere, temperature, nickel-carrier interactions, and dopants.* Applied Catalysis A: General, 2006. **309**: p. 237-246.
- 14. Sorensen, C.H.B.W.L., *Sintering kinetics of silica- and alumina-supported nickel in hydrogen atmosphere*. Journal of Catalysis, 1983. **81**(1): p. 131-141.
- 15. Crump, J.T.R.J.G., *Crystallite size distributions of sintered nickel catalysts.* Journal of Catalysis, 1979. **57**(3): p. 417-425.
- 16. Hsieh, C.H.B.M.V.S.H.-Y., Effects of Support on Carbon Formation and Gasification on Nickel during Carbon Monoxide Hydrogenation. Applied Catalysis, 1988. **36**: p. 147-162.
- 17. Schmal, A.L.A.M.M.V.M.S.M., Carbon formation and its influence on ethanol steam reforming over  $Ni/Al_2O_3$  catalysts. Catalysis Today, 2007. **123**(1–4,): p. 257-264.

- 18. Sanchez-Sanchez, M.C., et al., *Mechanistic Aspects of the Ethanol Steam Reforming Reaction for Hydrogen Production on Pt, Ni, and PtNi Catalysts Supported on γ-Al<sub>2</sub>O<sub>3</sub>.* The Journal of Physical Chemistry A, 2010. **114**(11): p. 3873–3882.
- 19. Kim, D., et al., Dynamic hydrogen production from ethanol steam-reforming reaction on  $Ni_xMo_y/SBA-15$  catalytic system. International Journal of Energy Research, 2015. **39**(2): p. 279–292.
- 20. Kang, S., B.S. Kwak, and M. Kang, Synthesis of Ni-alkaline earth metals particles encapsulated by porous  $SiO_2$  (NiMO@SiO<sub>2</sub>) and their catalytic performances on ethanol steam reforming. Ceramics International, 2014. **40**(9): p. 14197-14206.
- 21. Erdogan, B., H. Arbag, and N. Yasyerli, *SBA-15 supported mesoporous Ni and Co catalysts with high coke resistance for dry reforming of methane.* International Journal of Hydrogen Energy, 2018. **43**(3): p. 1396-1405.
- Bkour, Q., et al., *Synthesis and performance of ceria-zirconia supported Ni-Mo nanoparticles for partial oxidation of isooctane*. Applied Catalysis B: Environmental, 2017. **212**: p. 97-105.
- 23. Delgado, A.D., et al., Effect of the SiO<sub>2</sub> support morphology on the hydrodesulfurization performance of NiMo catalysts. Journal of Materials Research, 2018. **33**(21): p. 3646 3655.
- 24. Huirache-Acuña, R., et al., SBA-15 Mesoporous Silica as Catalytic Support for Hydrodesulfurization Catalysts—Review Materials, 2013. **6**(9): p. 4139-4167.
- 25. Bkour, Q., et al., Enhancing the partial oxidation of gasoline with Mo-doped Ni catalysts for SOFC applications: An integrated experimental and DFT study. Applied Catalysis B: Environmental, 2020. **266**: p. 118626.
- 26. Youn, M.H., et al., Role and effect of molybdenum on the performance of Ni-Mo/ $\gamma$ -Al $_2$ O $_3$  catalysts in the hydrogen production by auto-thermal reforming of ethanol. Journal of Molecular Catalysis A: Chemical, 2007. **261**(2): p. 276-281.
- 27. Huang, T.H.W., J. Huang, and P. Ji, *Methane reforming reaction with carbon dioxide over SBA-15 supported Ni–Mo bimetallic catalysts.* Fuel Processing Technology, 2011. **92**(10): p. 1868-1875.
- 28. Verma, P., et al., Functionalized mesoporous SBA-15 silica: recent trends and catalytic applications. Nanoscale, 2020. **12**(21): p. 11333-11363
- 29. Argyle, M.D. and C.H. Bartholomew, *Heterogeneous catalyst deactivation and regeneration: A review*. Catalysts, 2015. **5**(1): p. 145-269.
- 30. Elharati, M.A., et al., *Internal Reforming Solid Oxide Fuel Cell System Operating under Direct Ethanol Feed Condition*. Energy Technology Generation, Conversion, Storage, Distribution, 2020. **8**(9): p. 2000350.
- 31. Yin, Y., et al., Modification of as Synthesized SBA-15 with Pt nanoparticles: Nanoconfinement Effects Give a Boost for Hydrogen Storage at Room Temperature. Scientific Reports, 2017. **7**(1): p. 4509.
- 32. Zhang, T., X. Guo, and Z. Zhao, *Glucose-Assisted Preparation of a Nickel–Molybdenum Carbide Bimetallic Catalyst for Chemoselective Hydrogenation of Nitroaromatics and Hydrodeoxygenation of m-Cresol*. ACS Applied Nano Materials, 2018. **1**(7): p. 3579–3589.
- 33. El-Nahhal, I.M., et al., Synthesis and structural characterization of ZnO-and CuO-NPs supported mesoporous silica materials (hexagonal SBA-15 and lamellar-SiO<sub>2</sub>). Chemical Physics Letters, 2018. **691**: p. 211-218.
- 34. Erdem, B., et al., High-surface-area SBA-15–SO<sub>3</sub>H with enhanced catalytic activity by the addition of poly(ethylene glycol). Journal of Porous Materials, 2013. **20**: p. 1041–1049.
- 35. Li, Y., et al., *Grafting of Amines on Ethanol-Extracted SBA-15 for CO<sub>2</sub> Adsorption*. Materials, 2013. **6**(3): p. 981-999.
- 36. Mouli, K.C., et al., Effect of pore diameter of Ni–Mo/Al-SBA-15 catalysts on the hydrotreating of heavy gas oil. Applied Catalysis A: General, 2011. **404**(1–2): p. 21-29.

- 37. Vradman, L., et al., High loading of short WS<sub>2</sub> slabs inside SBA-15: promotion with nickel and performance in hydrodesulfurization and hydrogenation. Journal of Catalysis, 2003. **213**(2): p. 163-175.
- 38. Sundaramurthy, V., et al., *Hydrotreating of gas oil on SBA-15 supported NiMo catalysts.* Microporous and Mesoporous Materials, 2008. **111**(1–3): p. 560-568.
- 39. Phan, N.T.S. and C.W. Jones, *Highly accessible catalytic sites on recyclable organosilane-functionalized magnetic nanoparticles: An alternative to functionalized porous silica catalysts.* Journal of Molecular Catalysis A: Chemical, 2006. **253**(1–2): p. 123-131.
- 40. Bhaumik, A., S. Samanta, and N. KishorMal, *Highly active disordered extra large pore titanium silicate*. Microporous and Mesoporous Materials, 2004. **68**(1–3): p. 29-35.
- 41. Ngo, Y.-L.T. and S.H. Hur, Low-temperature NO<sub>2</sub> gas sensor fabricated with NiO and reduced graphene oxide hybrid structure. Materials Research Bulletin, 2016. **84**: p. 168-176.
- 42. Liao, X., et al., An in-depth understanding of the bimetallic effects and coked carbon species on an active bimetallic  $Ni(Co)/Al_2O_3$  dry reforming catalyst. Physical Chemistry Chemical Physics, 2016. **18**: p. 17311-17319.
- 43. Puech, P., et al., Analyzing the Raman Spectra of Graphenic Carbon Materials from Kerogens to Nanotubes: What Type of Information Can Be Extracted from Defect Bands? Journal of Carbon Research, 2019. **5**(4): p. 69.
- 44. Osswald, S., et al., *Elimination of D-band in Raman spectra of double-wall carbon nanotubes by oxidation*. Chemical Physics Letters, 2005. **402**(4–6): p. 422-427.
- 45. Dervishi, E., et al., *Raman spectroscopy of bottom-up synthesized graphene quantum dots: size and structure dependence.* Nanoscale, 2019. **11**: p. 16571-16581.